

The heating of dust by old stellar populations in the Bulge of M31

Brent Groves^{★1}, Oliver Krause¹, Karin Sandstrom¹, Anika Schmiedeke^{1,2},
Adam Leroy³, Hendrik Linz¹, Maria Kapala¹, Hans-Walter Rix¹,
Eva Schinnerer¹, Fatemeh Tabatabaei¹, Fabian Walter¹ and Elisabete da Cunha¹

¹Max Planck Institute for Astronomy, Königstuhl 17, D-69117 Heidelberg, Germany

²Universität zu Köln, Zùlpicher Strasse 77, 50937 Köln, Germany

³National Radio Astronomy Observatory, Charlottesville, VA 22903, USA

8 March 2013

ABSTRACT

We use new Herschel multi-band imaging of the Andromeda galaxy to analyze how dust heating occurs in the central regions of galaxy spheroids that are essentially devoid of young stars. We construct a dust temperature map of M31 through fitting modified blackbody SEDs to the Herschel data, and find that the temperature within 2 kpc rises strongly from the mean value in the disk of 17 ± 1 K to ~ 35 K at the centre. UV to near-IR imaging of the central few kpc shows directly the absence of young stellar populations, delineates the radial profile of the stellar density, and demonstrates that even the near-UV dust extinction is optically thin in M31’s bulge. This allows the direct calculation of the stellar radiation heating in the bulge, $U_*(r)$, as a function of radius. The increasing temperature profile in the centre matches that expected from the stellar heating, i.e. that the dust heating and cooling rates track each other over nearly two orders of magnitude in U_* . The modelled dust heating is in excess of the observed dust temperatures, suggesting that it is more than sufficient to explain the observed IR emission. Together with the wavelength dependent absorption cross section of the dust, this demonstrates directly that it is the optical, not UV, radiation that sets the heating rate. This analysis shows that neither young stellar populations nor stellar near-UV radiation are necessary to heat dust to warm temperatures in galaxy spheroids. Rather, it is the high densities of Gyr-old stellar populations that provide a sufficiently strong diffuse radiation field to heat the dust. To the extent which these results pertain to the tenuous dust found in the centres of early-type galaxies remains yet to be explored.

Key words: galaxies:individual:M31–galaxies:bulges–galaxies:ISM–infrared:galaxies

1 INTRODUCTION

As the nearest, massive galaxy, Andromeda (M31, NGC 224) has offered a unique insight into the properties of galaxies. It provides the perfect stepping stone between the well-resolved interstellar medium (ISM) and stellar populations within our own Galaxy, and the integrated properties of more distant galaxies. Due to its proximity (~ 780 kpc), Andromeda offers more than a resolved example of an early-type spiral galaxy, but can also be used to explore the interaction of the ISM and stars in early-type galaxies (ETGs) through its large, visually dominant bulge.

Andromeda’s bulge dominates the stellar luminosity and mass within the central 1.5 kpc ($R_{\text{eff}}(\text{bulge}) \sim 0.5 - 1.1$ kpc; Courteau et al. 2011), with the disk dominating beyond this. The bulge contributes $\sim 30\%$ of the total stellar mass and luminosity in M31, and it is clearly the highest surface brightness feature at UV –

NIR wavelengths (Geehan et al. 2006; Courteau et al. 2011). While the integrated colours and luminosity of M31 may place the galaxy in the “green valley” (Mutch et al. 2011), the optical colours of the bulge are red, with a $B - V \approx 0.9$ to 1.0 (Walterbos & Kennicutt 1987), placing it securely in the range of the red-sequence, where most early-type galaxies are found. Oke & Sandage (1968) even used the spectral energy distribution of the centre of M31 as a representative for the average giant elliptical galaxy when determining K -corrections.

This “early-type” nature of the bulge is supported by the old mean stellar age determined for the central region of M31. Resolved star colour-magnitude diagrams created by ground-based, adaptive-optics, NIR imaging reveal a population dominated by stars greater than 6 Gyr (Davidge et al. 2005; Olsen et al. 2006), while single-stellar population fits to absorption-line indices from slit-spectroscopy of the bulge (Saglia et al. 2010) find that the bulge of M31 is uniformly old (≥ 12 Gyr, excluding the central arcsecs). High-resolution, individual star photometry from

★ brent@mpia.de

the Pan-Chromatic Hubble Andromeda Treasury survey (PHAT; Dalcanton et al. 2012) find no population of young-stellar sources, with the UV-light dominated by evolved stars such as post-AGB stars (Rosenfield et al. in prep.).

Given this lack of young stars and star-formation, it is unsurprising that the bulge of M31 is also extremely gas poor. Little to no CO is detected in the CO(1-0) map of Nietten et al. (2006) down to low surface brightnesses. CO is detected in the central part of M31 when deeper observations of small high attenuation regions are made (Melchior et al. 2000; Melchior & Combes 2011), however the attenuation in these regions is still relatively low ($A_B < 0.3$) and the covering fraction of these regions is very small (Melchior et al. 2000), meaning diffuse, low attenuation dust (and presumably diffuse gas) is more characteristic of the bulge. Compounding this is a low CO-H₂ ratio (Leroy et al. 2011), and a low total HI column (Braun et al. 2009) giving a total cool gas mass in the centre of only a few $10^6 M_\odot$ ($\sim 0.02\%$ of the bulge stellar mass), likely dominated by molecular gas (e.g. Li et al. 2009; Melchior & Combes 2011).

This low gas fraction makes the M31 bulge more gas-poor than many ETGs, as recent work with the ATLAS3D sample (Cappellari et al. 2011) has demonstrated. Young et al. (2011) observed CO(1-0) in $\sim 22\%$ of the sample of nearby early-type galaxies, giving corresponding gas masses of $M(\text{H}_2) > 10^7 M_\odot$ (for a sample with a median stellar mass of $M_\star = 3 \times 10^{10} M_\odot$). Similarly, studies of nearby field ellipticals and lenticulars have found atomic gas in a large fraction of these ($\sim 70\%$), with this H I emission generally associated with ionized gas emission (Morganti et al. 2006). Interestingly, the molecular gas in early-type galaxies is not always associated with star formation. Optical colours and emission-line ratios indicate other forms of heating in the ISM of some early-types, and only low levels, if any, of star formation (Crocker et al. 2011).

Given the very low level of star formation, low attenuation, and small amount of gas at the centre of M31, little dust emission was expected in the central kiloparsecs of M31. Yet when this region was examined in the far-IR with IRAS (Habing et al. 1984), ISO (Haas et al. 1998), and *Spitzer* (Gordon et al. 2006), emission at wavelengths greater than $60 \mu\text{m}$ was clearly seen, indicating the presence of warm dust. In nearby ETGs, low-levels of warm dust are also being detected, with Smith et al. (2011) finding dust emission in 24% of ellipticals and 62% of S0s in the *Herschel* Reference survey. While M_{dust}/M_\star is far lower in spheroids than in disks, the dust appears to be warmer on average than that found in later-type galaxies. A similar result was found using *Herschel* in nearby early-type spirals similar to M31 by Engelbracht et al. (2010), with the mean dust temperature of the bulges consistently hotter than the disks in these galaxies. Relatively higher dust temperatures were also found by Rowlands et al. (2011) in the *Herschel*-ATLAS survey of more distant ellipticals. Hence dust, when detected, tends to be in a warmer state in spheroids than that found across the disks of later-type galaxies.

Given the high density of stars in bulges, stellar heating is the likeliest explanation for the observed warmer dust temperatures in ETGs. Yet the old stellar ages found in ETGs, and especially in the centre of M31, argue against the standard view that the IR luminosity and warm dust is a direct tracer of star formation (e.g. Kennicutt 1998). Based on the IRAS observations and the extremely weak UV observed using the Astronomical Netherlands Satellite (ANS; Coleman et al. 1980), Habing et al. (1984) put forward the argument that it is the high density of late-type giant stars that provide the strong enough radiation field to heat the dust. Based on *Herschel* PACS and SPIRE maps of M31 with unprecedented resolu-

Table 1. M31 positional data^a

M31 nucleus position ^b	00 ^h 42 ^m 44.35 ^s
(J2000)	+41°16′08.60″
Position angle of major axis	37.7°
Inclination	75°
Distance ^c	780 ± 40 kpc ^d
Distance modulus	24.46

^a Based on NED data and references where given.

^b (Evans et al. 2010), and verified in *Spitzer* IRAC 3.6 μm image.

^c Stanek & Garnavich (1998); Rich et al. (2005), see also NED for other determinations.

^d $1' = 227 \pm 12 \text{ pc}$ along major axis

tion (Krause et al., in prep.), we follow Habing et al. (1984) and use this high resolution to demonstrate how and by what stellar populations dust is heated in the bulge of this galaxy, and, by proxy, in the spheroids of other inactive early-type galaxies.

We briefly review the *Herschel* data and reduction in section 2, and discuss the FIR geometry and integrated properties of the M31 bulge in section 3. In section 4 we determine and discuss the mean dust temperature across M31 and in the centre, and determine the heating mechanism for the rise in dust temperature in the centre. We finish with the discussion and summary in sections 5 and 6. The global properties of M31 we assume throughout this paper are listed in Table 1.

2 DATA AND REDUCTION

The M31 *Herschel* data and their reduction are described and discussed in detail in Krause et al. (in prep.), so we only briefly review the data here.

M31 was imaged in all 6 *Herschel* photometric bands (PACS 70, 100, and 160 μm , and SPIRE 250, 350, and 500 μm) in slow parallel mode for a total time of ~ 24 hours. The images extend for $\sim 3^\circ \times 1^\circ$, centred slightly off-nucleus (at the P.A. given in Table 1), covering the main stellar disk of Andromeda, including the 10kpc ring.

All images were reduced to level one using HIPE version 6.0, and then used SCANAMORPHOS v12.0 (Roussel 2012) to produce the final images. As HIPE v6.0 was used, we converted the PACS images from flight model (FM), 5 to FM, 6 by dividing by the factors listed in PACS Photometer Point Source Flux Calibration Report v1.0, which are 1.119 (70 μm), 1.151 (100 μm), and 1.174 (160 μm) for the three PACS photometer bands, respectively. All images were converted to MJy sr⁻¹. Based on SPIRE Observers' manual v2.4¹, we used beam areas of 423 \square'' (250 μm), 751 \square'' (350 μm), and 1587 \square'' (500 μm) for the three SPIRE bands, respectively, to convert from Jy beam⁻¹ to MJy sr⁻¹.

The mean FWHM of the PACS and SPIRE Point Response Functions/beams are; $\sim 5.6''$ (70 μm), $\sim 6.8''$ (100 μm), $\sim 11.4''$ (160 μm), $18.2''$ (250 μm), $24.9''$ (350 μm), and $36.3''$ (500 μm), respectively, for the 20''/s scans used here (for full details of the correct point spread functions and beams, see the PACS² and SPIRE¹ Observer manuals). The actual images use pixels sizes of 1'' for all PACS bands and 6'', 10'', and 14'', for the respective SPIRE

¹ http://herschel.esac.esa.int/Docs/SPIRE/html/spire_om.html

² http://herschel.esac.esa.int/Docs/PACS/html/pacs_om.html

bands. When comparing bands, we convert all bands to the lowest resolution and pixel size using the convolution kernels provided by Aniano et al. (2011).

For all bands we have measured the noise and background as discussed in Krause et al. (in prep.). The ‘background’ in the images is a combination of both Galactic foreground and background galaxies, and is significant only in the SPIRE images. For simplicity, a uniform background in each band was assumed and subtracted from the image.

The measured noise for each band in the original images is; 3.17 MJy sr^{-1} ($70 \mu\text{m}$), 3.23 MJy sr^{-1} ($100 \mu\text{m}$), 2.29 MJy sr^{-1} ($160 \mu\text{m}$), 0.68 MJy sr^{-1} ($250 \mu\text{m}$), 0.46 MJy sr^{-1} ($350 \mu\text{m}$), and 0.20 MJy sr^{-1} ($500 \mu\text{m}$). When convolved and binned to lower resolutions, the noise per resolution element in each band is obviously reduced, with the effective resolution driven by the longest wavelength (e.g. $36.3''$ FWHM and $14''$ pixels at the $500 \mu\text{m}$ resolution).

3 THE BULGE OF M31: STARS, DUST, AND GAS

3.1 The Far-IR emission in Andromeda

In Figure 1 we show a RGB image of the full disk of Andromeda using the PACS $70 \mu\text{m}$, PACS $100 \mu\text{m}$, and SPIRE $250 \mu\text{m}$ bands. One of the things that stands out in this image, apart from the dusty ring, is the blue centre of the IR map, indicating a distinct rise in dust temperature towards the centre of M31.

The central kiloparsec bulge region (hereafter referring to a circular aperture of radius $4.405''$ (1 kpc), centred on the stellar peak defined in Table 1) is relatively weak in the SPIRE $250 \mu\text{m}$ band compared to the extended disk and star forming ring, but shows a relative excess in the PACS $70 \mu\text{m}$ band. The far-IR emission in this central region appears more circular and shows a spiral like pattern within.

3.2 The correlation of dust and gas

The spiral pattern can be seen in finer detail with Figure 2, where we show the PACS $70 \mu\text{m}$ and SPIRE $250 \mu\text{m}$ contours overlaid on the $H\alpha$ image of the central kiloparsecs from Devereux et al. (1994). As demonstrated by Li et al. (2009) using *Spitzer* data (particularly their Figures 6 and 8), the IR emission follows well the morphology of the $H\alpha$ emission. The correspondence is not linear between the $H\alpha$ and the two *Herschel* bands, with offsets between the $H\alpha$ peaks and IR peaks, but in general the same barred spiral pattern is seen. The two *Herschel* bands match very well with each other within the inner 0.5 kpc ($2.2''$) radius, but outside this the correspondence becomes weaker as the dust becomes cooler, and the PACS $70 \mu\text{m}$ emission merges with the noise. To the NW and SE of the image in Figure 2b) we can see the contribution of the disk appearing at the SPIRE $250 \mu\text{m}$ wavelengths.

The correspondence of the dust and ionized gas emission together suggest that the dust is associated with the gas and also likely to be in the same lower inclination thin disk spiral (Jacoby et al. 1985; Ciardullo et al. 1988). The offset between the peaks in the $H\alpha$ and the IR emission indicates the presence of cooler, denser gas associated with the dust, that is still too low in column density to be observed in H I or CO, with the weak and non-detections in CO of several higher attenuation regions in the centre by Melchior et al. (2000) and Melchior & Combes (2011) supporting this. As the gas emission indicates that most of the gas is in a diffuse state, and attenuation maps show an, on average, extremely low attenuation, it

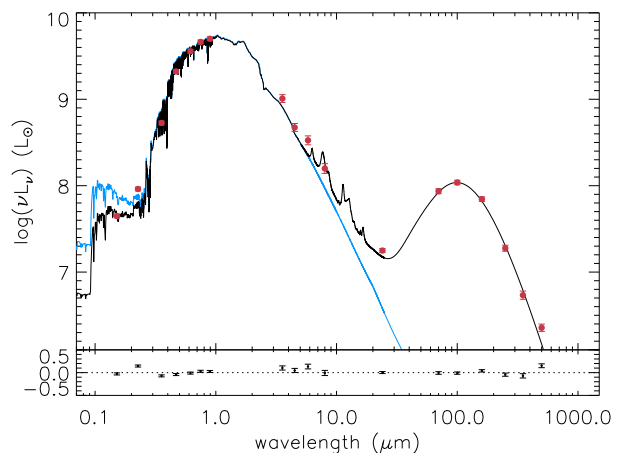


Figure 3. The spectral energy distribution (SED) of the central kpc region of Andromeda, measured within a circle of 1kpc ($4.405''$) radius from the centre. The fluxes (GALEX FUV and NUV, SDSS u , g , r , i , and z , *Spitzer* IRAC and MIPS24, and all six *Herschel* bands) within this aperture are marked by the red points, with the error bars including calibration, sky and noise uncertainties. The black curve shows the best fit model SED from the SED fitting code MAGPHYS (da Cunha et al. 2008), while the blue curve shows the corresponding unattenuated stellar SED from the same model. Below the model SED, the residuals between the observed data and models are shown, with $|\log(L_{\text{obs}}/L_{\text{mod}})| < 0.1$ dex for all wavelengths except for SPIRE500 μm , where the observed flux is under predicted by $\sim 30\%$.

is clear that the dust is likely to be optically thin to a significant amount of the radiation from the bulge stars.

3.3 The spectral energy distribution of the bulge

The low optical depth in the centre of M31 is also made clear by the full UV–IR SED in the central kiloparsec, which is illustrated in Figure 3, drawing on data from GALEX (Gil de Paz et al. 2007), SDSS (Aihara et al. 2011), *Spitzer* IRAC (Barmby et al. 2006) and MIPS (Gordon et al. 2006), and now *Herschel*. Overlaid on the observed data is the best fit from the SED fitting code MAGPHYS³ (da Cunha et al. 2008) (black curve) and its implied unattenuated stellar emission (blue curve). For this model fit we created a new stellar library using the original Bruzual & Charlot (2003) code and the same star formation histories as in da Cunha et al. (2008) but excluding all models which were formed less than 6 Gyrs ago ($t_g < 6 \text{ Gyr}$, see da Cunha et al. (2008), specifically §3.1.1), based on previous estimates for the mean stellar age of the bulge of M31 (see section 1, and e.g. Davidge et al. 2005; Olsen et al. 2006). The MAGPHYS model fit returns a stellar mass within this 1kpc radius of $\log(M_{\star}/M_{\odot}) = 10.01 \pm 0.01$, and an unattenuated stellar luminosity of $\sim 10^{9.9} L_{\odot}$. The dust luminosity of the M31 centre is $\sim 10^{8.3} L_{\odot}$, with MAGPHYS determining a total dust mass of only $\log(M_{\text{dust}}/M_{\odot}) = 5.17 \pm 0.05$.

As stated in the introduction, the $10^{10} M_{\odot}$ stellar mass of the bulge makes it a significant fraction ($\sim 30\%$) of the total stellar mass of M31 (Geehan et al. 2006). The optical–UV colours clearly reveal the old stellar age of the bulge, with $\text{NUV-}r \approx 5.0$. These colours lead to an extremely low estimated specific star formation rate from the model, with $\text{sSFR} < 0.01 \text{ Gyr}^{-1}$ ($\text{SFR} < 10^{-2} M_{\odot}$), in agreement with the lack of young stars observed in the bulge

³ www.iap.fr/magphys

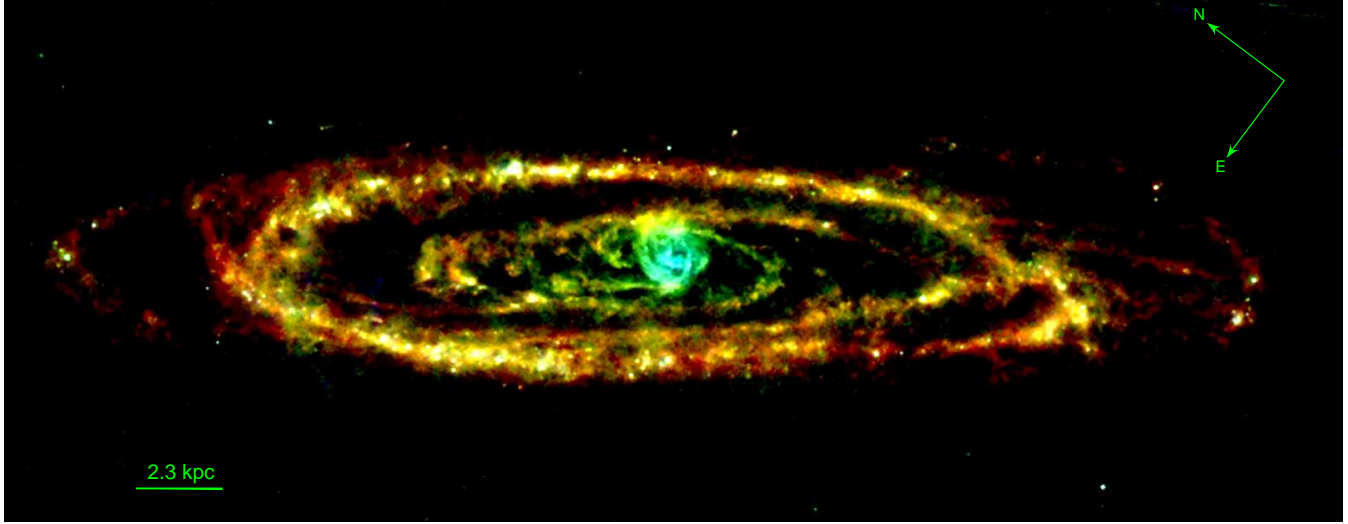


Figure 1. Far-infrared image of Andromeda using the Herschel bands showing PACS 70 μm (blue), PACS 100 μm (green), and SPIRE 250 μm (red), all convolved to SPIRE 250 μm resolution (from Krause et al., in prep.). All three bands have the same square root scaling from 10 MJy sr^{-1} to 150 MJy sr^{-1} . The angular scale of the image is shown by the 2.3 kpc ($10'$) bar in the lower left.

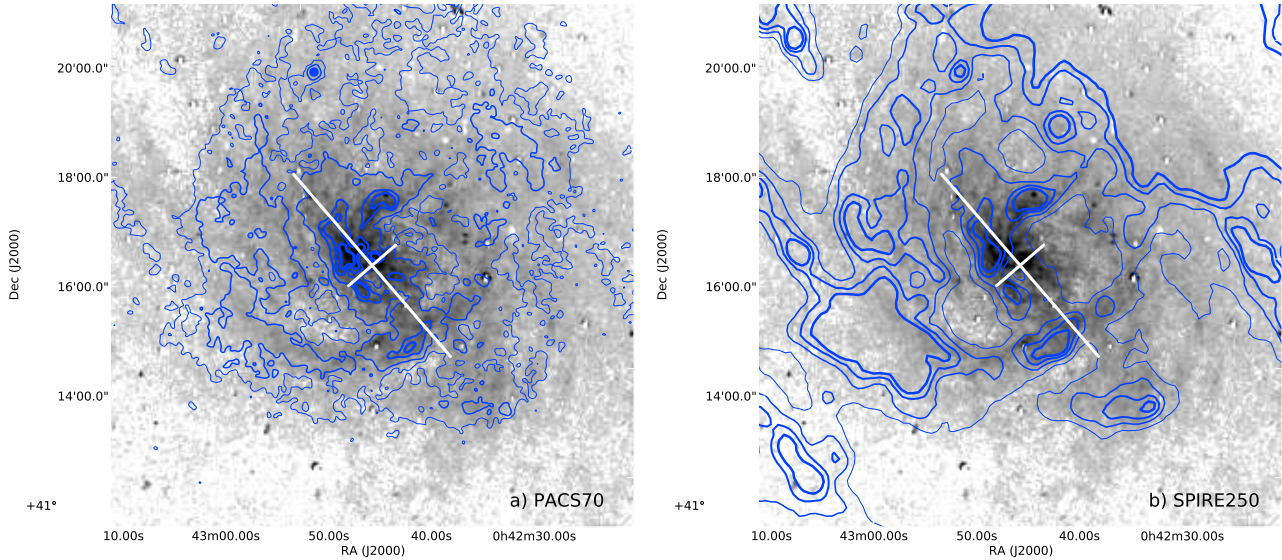


Figure 2. Continuum-subtracted $H\alpha$ + $[\text{NII}]$ narrow band image of the central kiloparsecs of M31 (greyscale) from Devereux et al. (1994) overlaid with contours from PACS 70 μm (left) and SPIRE 250 μm (right) imaging. In both images the $H\alpha$ has a square root stretch, and the centre is marked by a cross of 1 kpc length along both the major ($4.4'$) and minor axis ($1.14'$), assuming the inclination of M31 given in Table 1. For the PACS 70 μm contours, the levels are 15, 30, 70, and 100 MJy sr^{-1} , while for the SPIRE 250 μm contours, the levels are 10, 15, 20, and 25 MJy sr^{-1} , each indicated by an increasing thickness.

of M31. (Davidge et al. 2005; Olsen et al. 2006; Rosenfield et al. in prep.).

It should be noted that the values here for the dust mass and luminosity in the central kiloparsecs are likely upper limits for the dust in the bulge, as even at these small radii, some fraction of the IR emission still arises from the disk in the foreground and background due to the high inclination of Andromeda. This contribution of the disk infrared emission may also explain the weak UV ($< 0.25 \mu\text{m}$) excess observed in the unattenuated spectrum of the best fit MAGPHYS model relative to the observed SED. To explain the observed IR SED, the MAGPHYS model finds a small component of buried young stars necessary. This component is small (as demonstrated by the low sSFR), and cannot be associated with

the bulge (as the high-resolution observations have shown), but still contributes significantly to the unattenuated UV.

The total attenuation in the diffuse ISM is extremely low, as can be seen in the differences between the black and blue curves, with the model finding an attenuation in the diffuse ISM of only $\tau_V \sim 0.03$. The low value of attenuation measured from the SED matches that observed in B -band attenuation maps (Melchior et al. 2000), and is a result of a very low dust column, with the SED fit returning an average dust column density of only $\sim 4.5 \times 10^4 M_\odot \text{ kpc}^{-2}$ in the central region.

In contrast to the stellar mass, the bulge contributes little to the total dust mass in M31. At larger radii, emission from the disk of M31 along the minor axis overlaps with (and dominates over)

the dust emission from the bulge. Fits to the integrated IR spectral energy distribution (SED) of the Andromeda galaxy (within a 21.5 kpc aperture, Krause et al., in prep.), using both the Draine & Li (2007) and da Cunha et al. (2008) models, reveal that the dust mass in the inner 2kpc only contributes $\sim 0.5\%$ to the total dust mass of M31. However, the central 1 kpc contributes a ten-times larger fraction (i.e. $\sim 5\%$) to the total IR luminosity of M31, because of the relatively warmer dust emission. We can quantify the temperature of this dust in the bulge and in the rest of M31 by fitting simple modified blackbodies.

4 THE DUST HEATING IN THE M31 BULGE

4.1 Simple modified blackbodies

We now convert the spatially resolved thermal-IR SEDs into dust temperatures, describing the emission locally with a single dust temperature, T_d . While a simplification, this method returns a reasonable estimate for the mean, luminosity-weighted temperature of the dust.

We do this by using a simple modified blackbody;

$$S_\nu = N_d \kappa_{\nu 0} B_\nu(T_d) \left(\frac{\nu}{\nu_0} \right)^\beta, \quad (1)$$

where the dust surface brightness, S_ν , is proportional to the Planck function for the given dust temperature, $B_\nu(T_d)$, modified by the dust emissivity, which is assumed to be a power-law function of frequency, $\kappa_{\nu 0} (\nu/\nu_0)^\beta$. At a given dust temperature this is then simply multiplied by the dust column density, N_d , to yield the surface brightness.

The power-law function is a reasonable approximation for the dust emissivity (see e.g. Hildebrand 1983; Draine 2003), with the galactic diffuse ISM well fit by an emissivity index of $\beta = 2$ (Draine & Lee 1984). While a mean temperature for the dust can be determined, in reality there will be a range of temperatures along the lines-of-sight due to both a distribution of grain sizes and heating radiation fields (see, e.g. Draine & Li 2007). This simplified modelling foremost reflects a physically-motivated conversion of the FIR colours into the three parameters returned by the fitting procedure: T_d , β , and $N_d \kappa_{\nu 0}$. We refer to Shetty et al. (2009a,b) for a more detailed description of the issues and uncertainties in using simple modified blackbodies for integrated IR data.

We fit the modified blackbody to the 100-500 μm Herschel bands at the 500 μm resolution. We do not include the PACS 70 μm data due to the lower S/N across the M31 image, and as we expect the emission at these wavelengths to have a significant contribution from stochastically heated dust grains. We limit our fitting to all pixels with $S/N > 5$ in all 5 bands, which in practice is limited predominantly by the PACS 100 μm band. To fit the simple modified blackbody to the data, we assume a uniform, bounded prior grid for all three parameters, compute the χ^2 goodness of fit for every model parameter set j ,

$$\chi_j^2 = \sum_\nu \left(\frac{S_{\nu, \text{obs}} - S_{\nu, j}}{\sigma_\nu} \right)^2, \quad (2)$$

where $S_{\nu, \text{obs}}$ and σ_ν are the observed surface brightness and observational uncertainty for the band ν , respectively, and $S_{\nu, j}$ is the model flux for parameter set, j , determined from Equation 1. The bounds for dust temperature and emissivity were $5 < T_d < 50$ and $0.5 < \beta < 3.5$, respectively. We then determine the probability for each parameter set assuming a gaussian distribution, $\exp(-\chi_j^2/2)$,

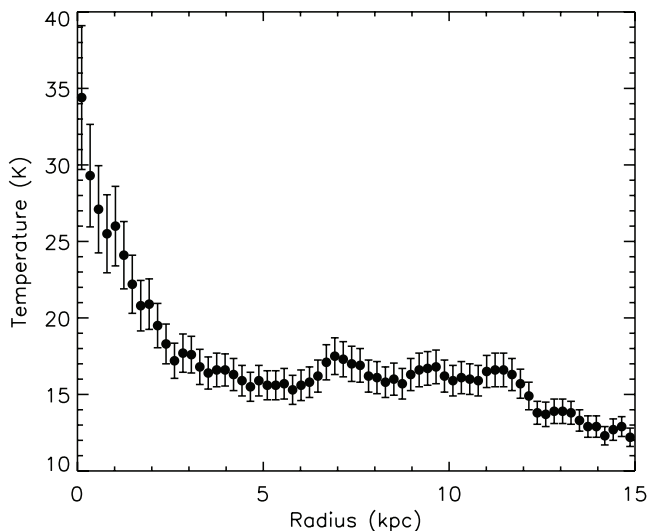


Figure 5. Radial variation of mean temperature in M31. The temperature is determined by fitting the median flux in all bands in radial bins of 230pc width using elliptical annuli. The error bars show the 16-84 percentiles of marginalised PDFs.

and marginalise over the other parameters to determine the probability distribution function (PDF) for each parameter, e.g. T_d . An examination of the PDF for T_d in several pixels shows a symmetric Gaussian distribution (as can be seen in the symmetric uncertainties in Figure 5), providing justification for our assumed Gaussian uncertainties for the parameters.

4.2 The dust temperature across M31

We performed this fit for every 14'' pixel in the M31 IR data that laid above our S/N cut, with the resulting image for the dust temperature shown in Figure 4. Pixels which fall below our S/N cut are shown as white, with the dust temperature (K) shown by the colour, as indicated by the colour-bar at the bottom of the image. Note that within 2 kpc, almost all pixels have sufficient S/N. The median temperature across the image is 17K, close to MIPS based disk temperature of 18 ± 1 K determined by Tabatabaei & Berkhuijsen (2010). The uncertainties (half the 16-84 percentiles, or 1σ if the uncertainties are Gaussian) range from 5 to 15%, with the largest uncertainties in regions at the lowest signal to noise and the central kiloparsec. The median uncertainty is $\sim 6\%$ (~ 1 K) dominated by the emission in the dusty, star-forming ring seen in GALEX and FIR images (e.g., Thilker et al. 2005).

Two things stand out in this temperature map: the almost constant temperature in the disk of M31, with $T_d = 17 \pm 1$ K, and the strong temperature increase in the central ~ 2 kpc. The temperature in the 10kpc ring of M31 is clearly not exactly constant, with warm spots occurring throughout the ring. These warm spots correspond with the locations of HII regions in the disk as determined by H α images (c.f. the H α maps of Devereux et al. 1994; Azimlu et al. 2011).

4.3 The radial dust temperature

The central dust temperature rise is more clearly quantified by taking the median SED in radial bins. To do so we determined the median flux in all bands in radial bins of 230 pc (using elliptical annuli with a P.A. = 37.7° and axis ratio of 0.26), and determined

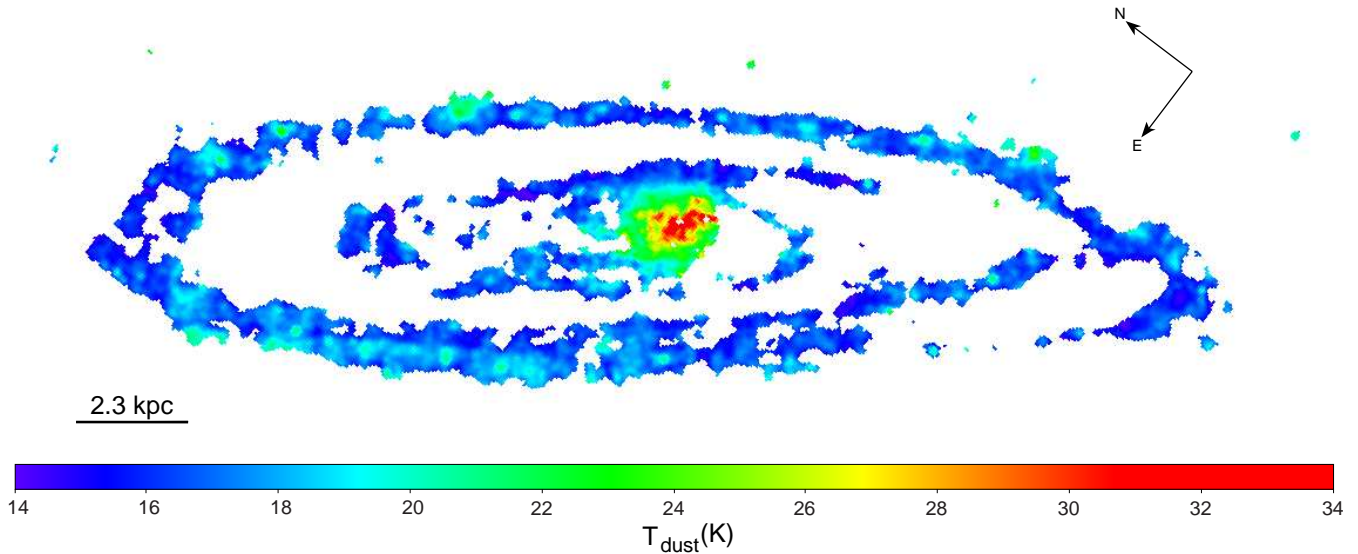


Figure 4. Effective dust temperature map of M31, determined from a single modified blackbody fit to each matched pixel of the PACS100, 160 μm and SPIRE 250, 350, and 500 μm bands, with all bands convolved to the SPIRE 500 μm PSF and resolution (as described in sections 4.1 and 4.2). The median temperature is 17K, and is dominated by the emission in the ring, while the highest temperature is reached in the nuclear region, as can be seen by the clear gradient in the figure. The median uncertainty is $\sim 1\text{K}$ or $\sim 6\%$.

the PDFs for all three parameters for each radial bin. The resulting temperature variation with radius is shown in Figure 5, with the 16–84 percentiles marked by the error bars. This plot clearly shows the marked increase in dust temperature in the inner 2kpc from the median disk dust temperature of $T_d = 16 - 17\text{K}$. The peak in dust temperature at the centre of $\sim 35\text{K}$ is similar to the dust temperature of $T_d = 33\text{K}$ determined by Soifer et al. (1986) for the central $4'$, using IRAS data and assuming a power law emissivity of $\beta = 2$. Similarly, Habing et al. (1984) found 34K (using $\beta = 1$) for approximately the same central region and same data. As these works use apertures of $4'$ diameter, to define the centre, these temperatures represent an average of the inner $\sim 0.35 - 0.45\text{kpc}$ and thus are remarkably close to our determined value. As these fits are based on only the IRAS 60 and 100 μm bands, and thus biased to the warmer dust temperatures due to the shorter wavelengths, the similarity in temperatures suggest that a single, warm component of dust dominates the IR SED in the centre. This is supported by the similarity of the PACS 70 μm flux and the model flux in the central kpc, even though not actually used to determine the fit.

In addition to giving access to the full IR SED, and thus a better measure of dust temperature, the higher resolution of *Herschel* enables us to see the steep gradient in temperature from the disk to the centre. This difference between the bulge and disk dust temperature in M31 agrees with what Engelbracht et al. (2010) found for the KINGFISH sample of nearby galaxies (Kennicutt et al. 2011). Engelbracht et al. (2010) found that the ratio of the central to disk dust temperature was greater than 1 across their sample, and increased with increasingly earlier types (see e.g. their Figure 3).

The emissivity, β , determined from these fits has a large uncertainty across M31, and is consistent with $\beta = 2$ at all radii. Given this, we created a higher resolution temperature map using only the 100, 160, and 250 μm bands with the assumption of a constant emissivity of $\beta = 2$. The resulting image of the central region is shown in Figure 6, where the central kiloparsec region is marked as a black circle and the median uncertainty is 0.75 K. Interestingly, while more structure in the temperature distribution in the centre is

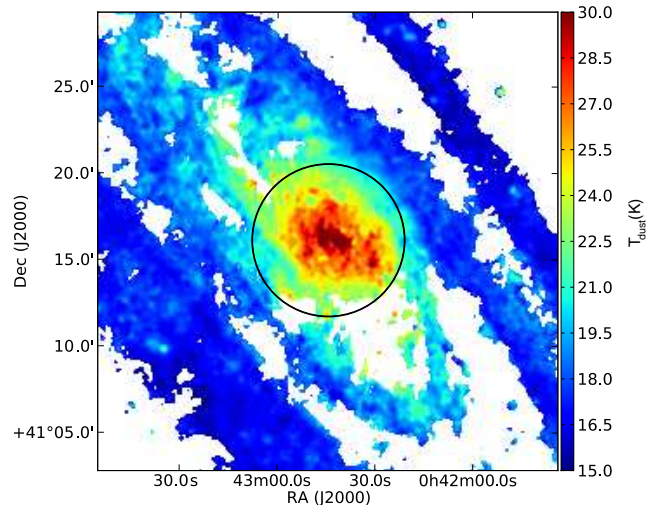


Figure 6. Effective dust temperature map of the central region of M31, determined from a single modified blackbody fit to each matched $6''$ pixel of the convolved PACS100, 160 and SPIRE 250 μm bands, assuming a constant emissivity of $\beta = 2.0$. The black circle outlines the central kiloparsec region.

seen due to the higher resolution, the overall temperature gradient in the centre still dominates the image. The steeper gradient in dust temperature along the minor axis arises from the mixture of disk dust emission with that from the bulge, leading to an overall lower average dust temperature in these regions. The fine scale structure is likely due to the distribution of the diffuse gas and dust as seen in Figure 2.

4.4 The heating mechanism of the bulge dust

The clear temperature increase in the central regions of M31 as seen in Figure 5 is interesting as it closely corresponds with the stellar

light distribution as traced by the near-IR emission, suggesting that the heating of the dust and bulge are linked. As Li et al. (2009) demonstrated (particularly their Figure 3c), both the H α and diffuse X-ray emission also increase toward the centre in the same manner as the stellar light. However, with the resolution offered by *Herschel* we can begin to understand the heating of the dust in the bulge of M31, and by proxy in the bulges of early type spirals and in early-type galaxies.

4.4.1 Potential heating sources

In principle, one possibility for heating the dust is a low level of star formation, buried amongst the dust and bulge stars. However, high resolution observations by HST show that no OB stars are apparent throughout the bulge (e.g. Brown et al. 1998; Rosenfield et al. in prep.), and no regions of high enough attenuation to bury such potential star formation are observed (Melchior et al. 2000). Also, the observed emission line ratios in the ionized gas (e.g. [N II]/H α) argue against young stars being the dominant heating mechanism (Ciardullo et al. 1988; Saglia et al. 2010).

As the super massive black hole at the centre of M31 (dubbed M31*) is quiescent (Li et al. 2011), heating by an AGN radiation field can be discounted. In addition, the radial profile of dust temperature is incompatible with a dominant central source heating, as shown in the following section.

Collisional heating of the dust by the hot 10^6 K X-ray gas at the centre of M31 (Li & Wang 2007) is another possibility (see, e.g. Voit 1991; Natale et al. 2010). However, the association of the dust with the H α emission and the weak detection of CO in regions of higher attenuation (discussed in section 3.2) indicate that the dust is in a denser medium, and not predominantly associated with the X-ray gas itself. Likewise, the total energy in the diffuse X-ray gas is insufficient to fully explain the H α emission, and thus is unlikely to heat the dust either (Li et al. 2009). Thus, while this may contribute to the emission, it is insufficient to explain the majority of the hot dust emission.

4.4.2 Bulge star heating

This leaves the high stellar density of old stars at the centre as the dominant heating mechanism of the dust in the bulge of M31, as originally suggested by Habing et al. (1984). By comparing the stellar light distribution for the bulge against the distribution of temperatures in the central kiloparsecs, we can now demonstrate the link between the heating of dust by the bulge and the dust emission. In the case of a simple steady-state temperature, grain cooling balances the dust heating, and the grain temperature is then proportional to (as shown in, e.g. Draine 2011, particularly Equations 24.17 and 24.18);

$$T_d = \left(\frac{h\nu_0}{k_B} \right)^{\beta/(4+\beta)} \left[\frac{\pi^4 \langle Q_{\text{abs}} \rangle_{\star} c}{60\Gamma(4+\beta)\zeta(4+\beta)Q_0\sigma} \right]^{1/(4+\beta)} U_*^{1/(4+\beta)}, \quad (3)$$

where Q_0 and $\langle Q_{\text{abs}} \rangle_{\star}$ are the dust absorption cross-section at the reference frequency ν_0 and averaged across the heating spectrum (Equation 24.2 in Draine 2011), respectively, Γ and ζ are the Gamma and Riemann zeta functions and U_* is the heating stellar radiation field density. In the simple assumption where the emissivity slope is constant at $\beta = 2$, this reduces to

$$T_d = \left(\frac{21h^2c}{160\pi^2k_B^2\sigma} \right)^{\frac{1}{6}} (\langle Q_{\text{abs}} \rangle_{\star,0} \nu_0^2 U_*)^{\frac{1}{6}}, \quad (4)$$

where $\langle Q_{\text{abs}} \rangle_{\star,0}$ is the spectrally-averaged dust absorption cross-section normalised at ν_0 . Using a reference wavelength of $\lambda_0 = 100 \mu\text{m}$ and the unattenuated spectral energy distribution determined in section 3.3, $\langle Q_{\text{abs}} \rangle_{\star,0} \sim 197$ for a Milky Way dust model with $R_V = 3.1^4$ (at $\lambda_0 = 250 \mu\text{m}$, $\langle Q_{\text{abs}} \rangle_{\star,0}$ is approximately $(2.5)^2$ larger; Draine 2003).

We can estimate the stellar radiation field heating the dust with a few simple assumptions: **1)** the dust is in a thin disk at the centre of M31 and **2)** is optically thin to the dominant heating radiation, and **3)** the bulge stellar mass is spherically distributed and **4)** has constant colours and stellar population. The first assumption is based on the findings given in section 3.2, where the correlation of ionized gas and dust suggest a thin disk geometry. The measured opacity in the bulge of M31 is low, as shown by Melchior et al. (2000), as is the average dust column of $\sim 4.5 \times 10^4 M_{\odot} \text{ kpc}^{-2}$ (see §3.3), thus the assumption of optically thin dust is not unreasonable. As for the third assumption, the bulge of M31 has already been shown to be non-symmetric, displaying a boxy structure, and possibly even different P.A. and inclination angle to the disk (e.g. Courteau et al. 2011). However, a simple spherical approximation for the bulge with a constant mass-to-light ratio can actually reasonably well reproduce the stellar light profile, as shown by Geehan et al. (2006). The NIR colours are close to constant as shown in Figure 1 in Courteau et al. (2011), but the UV colour, however, does show a gradient (see, e.g. Figure 3 in Thilker et al. 2005). While some of this may arise from a gradient in attenuation, there exists also radial gradients in the UV-emitting stellar populations (Rosenfield et al. in prep.) that may affect our assumptions (though the follow section argues against this).

As shown in Appendix A, given these assumptions, using the model for the bulge profile from Geehan et al. (2006) and the integrated unattenuated stellar luminosity from section 3.3, the bulge interstellar radiation field heating the dust is

$$U_*(r) = \frac{3.66 \times 10^{-11}}{(r/\text{kpc})} \int_0^{\infty} \frac{\ln \left(\frac{r/r_b + x}{|r/r_b - x|} \right)}{(1+x)^3} dx \text{ erg cm}^{-3}, \quad (5)$$

at a radius r (in kiloparsecs), and a bulge scale radius of $r_b = 0.61 \text{ kpc}$.

From Equations 4 and 5, we can then determine the expected dust temperature (given the above assumptions) as a function of spherical radius. For an infinitely thin disk, located in the plane of M31, we can equate the dust temperature in spherical coordinates with that in cylindrical (i.e. $r = R$, $z = 0$), giving

$$T_{d,U_*}(R) = 1750 [U_*(R)]^{\frac{1}{6}} \text{ K}, \quad (6)$$

where the factor 1750 arises from using the Milky Way dust model described above for $\langle Q_{\text{abs}} \rangle_{\star,0}$, and U_* is in erg cm^{-3} as in Equation 5.

In Figure 7 we show the distribution of the 6'' pixels from the dust map in Figure 6 in terms of the dust temperatures with distance from the centre, based on our simple circular radius. Overlaid on this distribution are two curves. The expected dust heating distribution, $T_{d,U_*}(R)$, as given by Equation 6, is shown by the dotted curve. As is clear from the figure, this is in excess of the observed temperature in M31's bulge. The solid curve shows the same $T_{d,U_*}(R)$, however multiplied by a factor 0.8. This brings it in agreement with the observed temperature distribution except at radii larger than $\sim 1.2 \text{ kpc}$. The first thing to take from these two curves is that the bulge provides a more than sufficient interstellar

⁴ Available from <http://www.astro.princeton.edu/~draine/dust/dustmix.html>

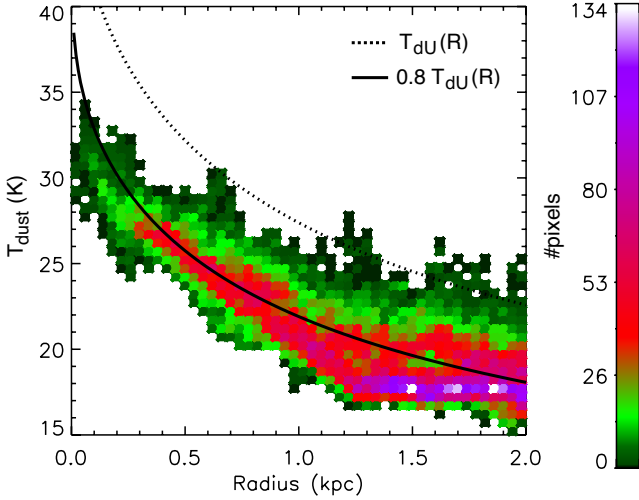


Figure 7. The distribution of dust temperatures within the inner 2 kpc (530'') of M31. The colours show the number density of the 6'' pixels from Figure 6 in terms of (T_d) and circular radius, as labelled by the colour bar to the right. Overlaid on this are two curves showing expected heating as based on the determined bulge ISRF. The dotted and solid curves show, respectively, the expected dust temperature distribution, $T_{d,U_*}(R)$, from Equation 6 and the same $T_{d,U_*}(R)$ scaled by 0.8.

radiation field (ISRF_b) to heat the dust, with expected temperatures in excess of that observed. However, importantly, the observed gradient in temperatures matches that expected from heating the bulge. This leaves the question, why is the expected temperature distribution in excess of that observed?

There are several possibilities given our simple assumptions. One possible explanation is suggested by the flattening of the T_{dust} pixel distribution in Figure 7 at radii > 1.3 kpc. This flattening is most likely due to the increasing disk contribution to the IR at these radii, which acts to lower the mean line-of-sight dust temperature. This is approximately the radius where the stellar mass distribution, and therefore light distribution, becomes disk dominated (see, e.g. Geehan et al. 2006; Courteau et al. 2011), and thus disk dust is likely also dominating the determined dust temperature. As discussed in section 4.2 and shown in Figure 4, the mean dust temperature across the disk is ~ 17 K, which is also where the pixel distribution flattens to in Figure 7. Figure 6 also gives some indication of the disk contribution to the bulge temperature, as there is clearly a flatter gradient of temperatures along the major axis as compared to the minor axis, which should have a greater contribution of disk dust due to the high inclination of M31. However, an examination of the observed IR SED within the central kiloparsec indicates that it is well described by a single black-body, as mentioned in section 4.3. As a confirmation we also fitted the pixel-SEDs in the central region with a combination of two modified-blackbodies. For both blackbodies, we assumed an emissivity of $\beta = 2$, and let the temperature of the first component free, and that of the second, cooler component constrained to 17 K. A simple fit found that the central kpc region is dominated by the warmer component, whose temperature distribution is almost indistinguishable from Figure 7. Thus, while it must occur at radii > 1 kpc, the contribution of the disk cannot explain the offset between the theoretical curve and the observational-based temperature.

Another possibility is that the dust in the bulge is not Milky Way like, and our assumed $\langle Q_{\text{abs}} \rangle_{*,0}$ is incorrect. For example, if we assume a Milky Way model of dust, but with $R_V = 5.5$ (using

the (Weingartner & Draine 2001) model opacity), $\langle Q_{\text{abs}} \rangle_{*,0}$ reduces to ~ 155 (normalised at $\lambda_0 = 100 \mu\text{m}$, as above). Such a possibility is reasonable, given that the extreme environs of the bulge may act to alter the dust size distribution, destroying small grains leading to a flatter opacity. However, given the index of 1/6 in Eqn. 4, the offset in temperature requires a significant change in dust opacity if this alone causes this offset. Similarly, our estimate of U_* is also likely incorrect given that the bulge is not spherical (Courteau et al. 2011), and the dust is not in a perfectly thin disk. However, the index of 1/6 again requires our U_* to be over estimated by approximately an order of magnitude if it alone is incorrect.

More likely, it is a combination of these, plus the possibility of some self-shielding by dust (which acts to reduce the U_* seen by the dust), which lead to the difference between the theoretical temperature distribution and that determined from the modified blackbody fit to the data. Yet it should still be noted, that these are all needed to reduce the theoretical heating to that observed. The bulge stellar radiation field provides more than sufficient energy to heat the warm dust at the centre of M31.

As a final check that the bulge stars are dominating the heating, we can apply the same methodology and reasoning as used for Eqn. 4, but assuming that the radiation field heating the dust arises from a central point source (i.e. AGN or nuclear star cluster), meaning that $U \propto r^{-2}$. However, when $T_{d,U_*}(R)$ is determined for this radiation field (similar to Eqn. 6), the slope does not show the same form as in Figure 7, demonstrating that the heating radiation field must be extended. Even allowing for a greater contribution of the disk emission to approximate the observed slope, to match the point source $T_{d,U_*}(R)$ to the measured T_d requires a central luminosity that would be obvious in the optical (or X-ray) emission, which is discounted by observations as already discussed (Li et al. 2009).

4.5 The heating of dust by old stars

While Figure 7 clearly links the bulge with the dust emission, it does not reveal what exactly is heating the dust. Typically, due to the steep wavelength dependence of the dust opacity, the dust IR emission has been associated with UV light and hence star formation. Typically, diffuse dust is considered to be heated by a local interstellar radiation field (ISRF) or scaling thereof (see e.g. Draine & Li 2007). As this ISRF is typically based on the local ISRF of Mathis et al. (1983), the UV light dominates the heating of dust (e.g. Figure 4 in Mathis et al. 1983), and as the local UV light is dominated by B stars, the diffuse dust emission indirectly traces B stars and thus star formation on longer (~ 100 Myr) timescales. As shown by Thilker et al. (2005), the UV light strongly peaks at the centre of M31. However this UV light in the bulge has been shown to be not associated with star-formation, but rather arises from extreme horizontal branch stars (Brown et al. 1998; Rosenfield et al. in prep.).

However, while these hot, low-mass stars may be the source of the UV upturn and possibly the H α emission, they cannot be the dominant heating source of the dust. Based on the IRAS and ANS observations, Habing et al. (1984) realised that the UV light would not be sufficient to heat the dust, and the heating would be dominated by the $\lambda > 300$ nm light from evolved stars. In Figure 8, we show three panels that illustrate which radiation heats the dust. In the top panel we take the ‘‘unattenuated SED’’ from Figure 3, which is likely an overestimate at $\lambda < 0.25 \mu\text{m}$ (see Section 3). The middle panel shows the total dust absorption cross-section per gram of dust for the MW dust model with $R_V = 3.1$ from Draine (2003), as also used in the previous section. By multiplying these together

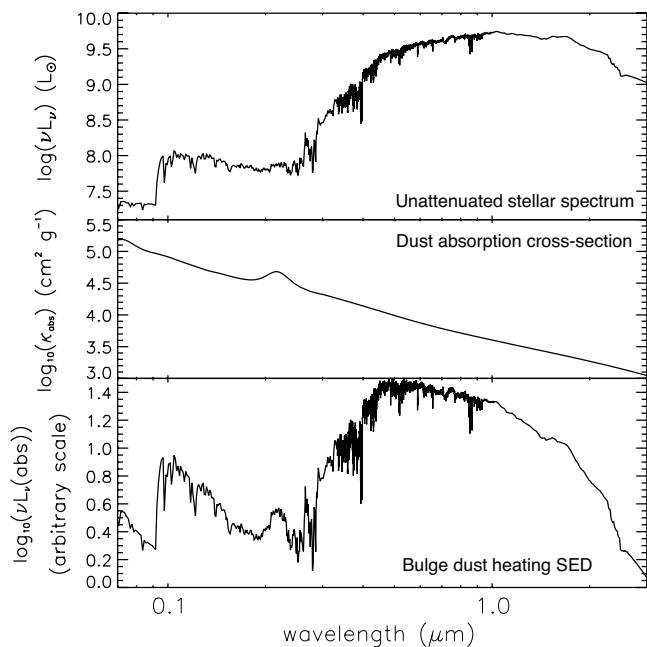


Figure 8. The energy absorbed by diffuse dust in the bulge of M31. The top panel shows the “unattenuated” bulge UV–NIR SED from the MAGPHYS (da Cunha et al. 2008) model fit to the integrated SED of the central kiloparsecs (blue curve in Figure 3). The middle panel shows the total absorption cross-section per gram of dust for the MW dust model with $R_V = 3.1$ from Draine (2003). The bottom panel shows the product of these, revealing the wavelength distribution of the energy absorbed by dust. The conclusion is that the optical stellar light is the main contributor to the dust heating in the bulge.

we obtain the amount of energy absorbed per H atom as a function of wavelength (bottom panel). This Figure reveals that most of the energy that heats the dust arises from optical photons, not the UV. As the $Q_{\text{abs}}(\nu)$ slope is ≈ 1 , the UV-optical slope needs to be < -1 (in frequency) for optical photons to dominate the heating of dust.

As mentioned before, the bottom panel of Figure 8 most likely overemphasises the role of UV photons in the heating due to the small UV excess in the model stellar SED (blue curve in Figure 3). The intrinsic UV emission produced by the evolved stars in the centre of M31 (the so-called UV-upturn observed in early-type galaxies) is well-reproduced by the Bruzual & Charlot (2003) code, as shown by a comparison of models with the observed UV colours of early-type galaxies (see specifically Figure 5 in Donas et al. 2007). Even if the model UV is incorrect, the intrinsic UV flux would still need to increase by ~ 0.4 dex (or 0.7 dex from the observed value) to be commensurate with the energy deposited in the optical. This lack of UV heating is also clear when the top panel of Figure 8 is compared with the ISRF of Mathis et al. (1983) (e.g. their Figure 1). When normalised to the peak at $\sim 1 \mu\text{m}$ (in both radiation fields), the UV in the ISRF is approximately an order of magnitude greater than that determined in M31.

Furthermore, the hot environment of the circumnuclear region of M31 may destroy the smallest dust grains as discussed in the previous section. The destruction of small grains flattens the slope of $\kappa_{\text{abs}}(\nu)$, leading to yet a greater dominance of optical photons in the dust heating. Thus the bulge of M31 is a clear case where the heating of dust is dominated by the light from old stars. This is in stark contrast to typical star-forming galaxies, where the UV from young stars dominates the heating of dust (e.g. Law et al.

2011). Montalto et al. (2009) had already found with GALEX–Spitzer data that the dust in the Andromeda galaxy as a whole appears to be heated mainly by stars a few Gyrs old. Habing et al. (1984) already inferred that the bulge of M31 takes this further with heating likely dominated by evolved stars. However, the mean stellar age of the bulge of M31 is > 6 Gyr, with some estimates placing the dominant age ≥ 10 Gyr (Davidge et al. 2005; Brown 2009; Saglia et al. 2010), demonstrating that even the oldest stars are able to heat dust. This is a clear cautionary note against using warm IR emission as a direct tracer of star formation, or obscured UV emission.

5 DISCUSSION

As the nearest massive galaxy, the Andromeda galaxy allows us to connect the small scale physics with the integrated properties of galaxies. The central kiloparsec of M31 actually matches very well many of the observed properties of nearby early-type galaxies. Within a 1 kiloparsec ($4.4'$) circular aperture the estimated stellar mass is $\sim 10^{10} M_{\odot}$, with a very old, red stellar light, estimated to be greater than 10 Gyrs old (Saglia et al. 2010). The optical colours of the bulge, e.g. $\text{NUV}-r \approx 5.0$, place it well in the realm of gas poor early-type galaxies (see, e.g. Oke & Sandage 1968; Saintonge et al. 2011; Smith et al. 2011).

There is a low level of dust attenuation across the centre, visible in both the difference between the observed and modelled intrinsic SEDs in Figure 3 and in the A_B map (their Figure 1) of Melchior et al. (2000). This low level of attenuation is a result of the low dust column across the centre and connected to the relatively weak IR emission. The total dust mass within this aperture from the da Cunha et al. (2008) MAGPHYS model is $10^{5.2} M_{\odot}$, contributing only 0.5% of the total dust mass to M31. However, the bulge contributes $\sim 5\%$ of the total IR luminosity due to the relatively warm, blue FIR emission. This dust mass results in a very low $M_{\text{dust}}/M_{\star}$ for the bulge, with $\sim 10^{-4.7}$. This actually places the bulge of M31 in a similar regime as the sample of early-type galaxies explored in the *Herschel* reference survey (HRS, Boselli et al. 2010) in Smith et al. (2011), falling somewhat in between the S0 and E galaxies (see their Figure 8). Similarly, the temperature increase from disk to bulge in M31 follows the trend of having warmer dust in earlier Hubble-types, as observed by Engelbracht et al. (2010) in the KINGFISH sample. This trend was also seen by Smith et al. (2011) in the HRS, who found warmer dust in E galaxies than S0, and an overall warm dust temperature for the sample (mean $T_d = 24\text{K}$).

The M_{gas}/M_{\star} ratio is also very low in the bulge of M31, with little H I and CO detected in the centre. However, ionized gas is seen in H α and the FIR emission is spatially well-correlated with this gas showing a similar lower inclination, barred-spiral pattern as visible in Figure 2, with the MIR emission also following the diffuse H α morphology (Li et al. 2009). Given this correlation, the H α emission allows the structure of the dust distribution to be determined (e.g. Jacoby et al. 1985), and indicates that the ISM in the centre, including the dust, is in a thin, spiral disk. The origin of this gas and dust in the centre of M31 is still not known, and beyond the scope of this work. Li et al. (2009) suggest that the stellar ejecta are more than sufficient to replenish the observed hot gas in M31’s centre, and suggest the rest of this matter comes out as a hot, X-ray flow. However, the spiral pattern observed in the bulge does appear to link up with the emission in the disk (Figure 1), even if it appears to be at a different inclination to the disk.

Given the above similarities using the bulge of M31 as a resolved representative of the spheroids of other early-type galaxies is a reasonable assumption. Based on this and our resolved study of dust heating in the bulge we can extrapolate to infer that a similar heating mechanism for the dust occurs in the majority of early-type galaxies in which dust is detected (i.e., the Smith et al. (2011) sample). While many early-type galaxies do have some AGN activity in the centre, and several, generally with higher gas masses, have observed active star formation (e.g. Crocker et al. 2011), the combination of diffuse, optically thin dust and a strong, diffuse radiation field due to the high stellar density is able to heat dust at the centres of these early-type galaxies to a significantly warmer level than that observed in most stellar disks. This increased dust temperature makes the generally dust poor early-types still visible in the recent and ongoing FIR surveys with *Herschel*.

However, the possible contribution of disk dust to the observed IR emission, as derived from the dust temperature offset in Figure 7, suggests a final cautionary note in this extrapolation. The bulge of M31 lies in a far different environment to typical early-type galaxies, which affects both the observed emission, and the evolution of the ISM in this early-type spheroid.

6 SUMMARY

When observed in the far-infrared, the bulge of the Andromeda galaxy (M31, NGC 224) stands out as a region of luminous blue emission (i.e. $70\mu\text{m}$ bright), surrounded by ring-like red emission from the disk. This corresponds to a peak in the mean dust temperature, T_d (Figure 4). Across the disk of M31, the mean dust temperature is reasonably constant with $T_d = 17 \pm 1\text{K}$. However, within the central kiloparsec, the temperature of the dust rapidly increases, reaching $T_d \sim 35\text{K}$ at the centre, as seen in Figure 5.

The start of this upturn is also where the bulge begins to dominate the stellar radiation field, clearly indicating that the heating mechanism of this warm dust and the bulge are associated. Heating by either an AGN or gas-grain collisions is discounted by X-ray observations, leaving stellar heating as the likely source. The radial profile of this steep increase in temperature in the inner kiloparsecs corresponds well with the temperature slope expected from heating by the diffuse radiation field arising from the bulge stars, suggesting direct link. The theoretical dust temperature based on the diffuse radiation field and our assumptions is actually in excess of that observed, providing more than sufficient heating. This excess suggests the not unreasonable possibilities of different dust properties in the bulge from the standard diffuse dust in the Milky Way and that the dust is likely to be in a clumpy distribution with some self-shielding occurring.

However, even though the bulge of M31 is observed in the UV, no young stars are seen in HST observations or spectra (Rosenfield et al. in prep.; Saglia et al. 2010), leaving old ($> 6\text{Gyr}$) stars as the dominant heating mechanism. Furthermore, by taking the observed SED of the bulge and standard dust opacity it is clear that it is the red optical light of these old stars that dominates the heating of the warm dust in the centre, as originally suggested by Habing et al. (1984) with the IRAS observations.

Together this demonstrates the possibility of heating dust by stars > 10 billion years old. This is one of the clearest demonstrations of how IR emission does not always correlate with star formation, a common assumption, but rather is dependent upon the distribution of dust (and associated gas) and the total radiation field, which includes both young and old stars. The bulge of M31 also

demonstrates one of the plausible mechanisms for heating the relatively warm dust observed in the centres of early-type spirals, and early-type galaxies.

ACKNOWLEDGEMENTS

The authors would like to thank P. Barmby and K. Gordon for providing the *Spitzer* IRAC and MIPS data for M31, respectively. B.G. would also like to thank R. Shetty, A. Stutz, G. Seidel, and G. van der Ven for interesting and helpful discussions. F.S.T. acknowledges the support by the DFG via the grant TA 801/1-1. This work made use of the NASA Extragalactic Database, and the IDL astro library routines.

REFERENCES

- Aihara, H., Allende Prieto, C., An, D., et al. 2011, *ApJS*, 193, 29
- Aniano, G., Draine, B. T., Gordon, K. D., & Sandstrom, K. 2011, *PASP*, 123, 1218
- Azimlu, M., Marciniak, R., & Barmby, P. 2011, *AJ*, 142, 139
- Barmby, P., et al. 2006, *ApJ*, 650, L45
- Boselli, A., Eales, S., Cortese, L., et al. 2010, *PASP*, 122, 261
- Braun, R., Thilker, D. A., Walterbos, R. A. M., & Corbelli, E. 2009, *ApJ*, 695, 937
- Brown, T. M., Ferguson, H. C., Stanford, S. A., & Deharveng, J.-M. 1998, *ApJ*, 504, 113
- Brown, T. M. 2009, *Galaxy Evolution: Emerging Insights and Future Challenges*, 419, 110
- Bruzual, G., & Charlot, S. 2003, *MNRAS*, 344, 1000
- Cappellari, M., Emsellem, E., Krajnović, D., et al. 2011, *MNRAS*, 413, 813
- Ciardullo, R., Rubin, V. C., Ford, W. K., Jr., Jacoby, G. H., & Ford, H. C. 1988, *AJ*, 95, 438
- Coleman, G. D., Wu, C.-C., & Weedman, D. W. 1980, *ApJS*, 43, 393
- Courteau, S., Widrow, L. M., McDonald, M., et al. 2011, *ApJ*, 739, 20
- Crocker, A. F., Bureau, M., Young, L. M., & Combes, F. 2011, *MNRAS*, 410, 1197
- da Cunha, E., Charlot, S., & Elbaz, D. 2008, *MNRAS*, 388, 1595
- Dalcanton, J. J., Williams, B. F., Lang, D., et al. 2012, *arXiv:1204.0010*
- Davidge, T. J., Olsen, K. A. G., Blum, R., Stephens, A. W., & Rigaut, F. 2005, *AJ*, 129, 201
- Devereux, N. A., Price, R., Wells, L. A., & Duric, N. 1994, *AJ*, 108, 1667
- Draine, B. T., & Lee, H. M. 1984, *ApJ*, 285, 89
- Draine, B. T. 2003, *ARA&A*, 41, 241
- Draine, B. T., & Li, A. 2007, *ApJ*, 657, 810
- Draine, B. T. 2011, *Physics of the Interstellar and Intergalactic Medium* by Bruce T. Draine. Princeton University Press, 2011. ISBN: 978-0-691-12214-4,
- Donas, J., Deharveng, J.-M., Rich, R. M., et al. 2007, *ApJS*, 173, 597
- Evans, I. N., et al. 2010, *ApJS*, 189, 37
- Engelbracht, C. W., Hunt, L. K., Skibba, R. A., et al. 2010, *A&A*, 518, L56
- Geehan, J. J., Fardal, M. A., Babul, A., & Guhathakurta, P. 2006, *MNRAS*, 366, 996

Gil de Paz, A., Boissier, S., Madore, B. F., et al. 2007, *ApJS*, 173, 185

Gordon, K. D., et al. 2006, *ApJ*, 638, L87

Haas, M., Lemke, D., Stickel, M., Hippelein, H., Kunkel, M., Herbstmeier, U., & Mattila, K. 1998, *A&A*, 338, L33

Habing, H. J., Miley, G., Young, E., et al. 1984, *ApJ*, 278, L59

Hernquist, L. 1990, *ApJ*, 356, 359

Hildebrand, R. H. 1983, *QJRAS*, 24, 267

Ferguson, A. M. N., et al. 2005, *ApJ*, 634, 287

Jacoby, G. H., Ford, H., & Ciardullo, R. 1985, *ApJ*, 290, 136

Kennicutt, R. C., Jr. 1998, *ARA&A*, 36, 189

Kennicutt, R. C., Calzetti, D., Aniano, G., et al. 2011, *PASP*, 123, 1347

Law, K.-H., Gordon, K. D., & Misselt, K. A. 2011, *ApJ*, 738, 124

Leroy, A. K., Bolatto, A., Gordon, K., et al. 2011, *ApJ*, 737, 12

Li, Z., & Wang, Q. D. 2007, *ApJ*, 668, L39

Li, Z., Wang, Q. D., & Wakker, B. P. 2009, *MNRAS*, 397, 148

Li, Z., Garcia, M. R., Forman, W. R., et al. 2011, *ApJ*, 728, L10

Mathis, J. S., Mezger, P. G., & Panagia, N. 1983, *A&A*, 128, 212

Melchior, A.-L., Viallefond, F., Guélin, M., & Neininger, N. 2000, *MNRAS*, 312, L29

Melchior, A.-L., & Combes, F. 2011, *arXiv:1103.3392*

Montalto, M., Seitz, S., Riffeser, A., et al. 2009, *A&A*, 507, 283

Morganti, R., de Zeeuw, P. T., Oosterloo, T. A., et al. 2006, *MNRAS*, 371, 157

Mutch, S. J., Croton, D. J., & Poole, G. B. 2011, *ApJ*, 736, 84

Natale, G., Tuffs, R. J., Xu, C. K., et al. 2010, *ApJ*, 725, 955

Nieten, C., Neininger, N., Guélin, M., et al. 2006, *A&A*, 453, 459

Oke, J. B., & Sandage, A. 1968, *ApJ*, 154, 21

Olsen, K. A. G., Blum, R. D., Stephens, A. W., et al. 2006, *AJ*, 132, 271

Rich, R. M., Corsi, C. E., Cacciari, C., Federici, L., Fusi Pecci, F., Djorgovski, S. G., & Freedman, W. L. 2005, *AJ*, 129, 2670

Rosenfield, P. & PHAT Team 2012, *ApJ*, in prep.

Roussel, H. 2012, *A&A*, submitted

Rowlands, K., Dunne, L., Maddox, S., et al. 2011, *MNRAS*, 1996

Saglia, R. P., Fabricius, M., Bender, R., et al. 2010, *A&A*, 509, A61

Saintonge, A., Kauffmann, G., Kramer, C., et al. 2011, *MNRAS*, 415, 32

Shetty, R., Kauffmann, J., Schnee, S., Goodman, A. A., & Ercolano, B. 2009a, *ApJ*, 696, 2234

Shetty, R., Kauffmann, J., Schnee, S., & Goodman, A. A. 2009b, *ApJ*, 696, 676

Smith, M. W. L., Gomez, H. L., Eales, S. A., et al. 2011, *arXiv:1112.1408*

Soifer, B. T., Rice, W. L., Mould, J. R., et al. 1986, *ApJ*, 304, 651

Stanek, K. Z., & Garnavich, P. M. 1998, *ApJ*, 503, L131

Tabatabaei, F. S., & Berkhuijsen, E. M. 2010, *A&A*, 517, A77

Thilker, D. A., Hoopes, C. G., Bianchi, L., et al. 2005, *ApJ*, 619, L67

Walterbos, R. A. M., & Kennicutt, R. C., Jr. 1987, *A&AS*, 69, 311

Weingartner, J. C., & Draine, B. T. 2001, *ApJ*, 548, 296

Voit, G. M. 1991, *ApJ*, 379, 122

Young, L. M., Bureau, M., Davis, T. A., et al. 2011, *MNRAS*, 414, 940

APPENDIX A: THE BULGE RADIATION FIELD

For the bulge radiation field we first need the stellar luminosity distribution (which we label $\nu_*(r)$). For this we follow Geehan et al.

(2006) and use a Hernquist (1990) mass profile due to its simple spherical geometry and assume a constant mass-to-light ratio, giving;

$$\nu_*(r) = \frac{L_b}{2\pi r_b^3} \frac{1}{(r/r_b)(1+r/r_b)^3}. \quad (A1)$$

Geehan et al. (2006) found the bulge radius to be 0.61 kpc (their Equation 1 and Table 2), and we used the determined unattenuated stellar luminosity within 1 kpc of $L_* \approx 10^{9.9} L_\odot$ (from section 3.3) to normalise L_b to $10^{10.32} L_\odot$.

The interstellar radiation field in the bulge (ISRF_b) is then simply the luminosity density (in e.g. $L_\odot \text{pc}^3$) convolved with spherical dilution, $1/r^2$;

$$\begin{aligned} U_*(r) &= \nu_*(r) * \frac{1}{4\pi r^2 c} \\ &= \int_V \nu_*(r_0) \frac{1}{4\pi(\vec{r}_0 - \vec{r})^2 c} dV, \end{aligned} \quad (A2)$$

where the factor $1/c$ is introduced to convert the ISRF_b to an energy density (i.e. erg cm^{-3}). As both the luminosity density and dilution are purely radial functions, the volume integral in Equation A2 reduces to (in spherical coordinates);

$$\begin{aligned} U_*(r) &= \int_0^\infty \frac{\nu_*(r_0)}{4\pi c} \int_0^{2\pi} \int_0^\pi \frac{r_0^2 \sin \phi}{r_0^2 - 2rr_0 \cos \phi + r^2} d\phi d\theta dr_0 \\ &= \int_0^\infty \nu_*(r_0) \frac{r_0}{2rc} \ln \left(\frac{r+r_0}{|r-r_0|} \right) dr_0. \end{aligned} \quad (A3)$$

Substitution of Eqn. A1 into this and condensing then gives

$$U_*(r) = \frac{L_b}{4\pi r_b c} \frac{1}{r} \int_0^\infty \frac{\ln \left(\frac{r/r_b + x}{|r/r_b - x|} \right)}{(1+x)^3} dx, \quad (A4)$$

where x has been substituted for r_0/r_b . The factor in front of $1/r$ and the integral equals $3.66 \times 10^{-11} \text{ erg cm}^{-3}$ for our given L_b and r_b , with r in kiloparsecs. While the integral in Eqn. A4 can be analytically determined, we use a numerical integration for simplicity within this work.